Available online at www.sciencedirect.com
ScienceDirect
Acta Materialia 57 (2009) 4809–4821
Acta MATERIALIA
www.elsevier.com/locate/actamat

Early pore formation in aluminium foams studied by synchrotron-based microtomography and 3-D image analysis

A. Rack [a,*], H.-M. Helwig [b,c], A. Bütow [b,c], A. Rueda [b,c], B. Matijašević-Lux [b,c], L. Helfen [d], J. Goebbels [e], J. Banhart [b,c]

[a] European Synchrotron Radiation Facility, F-38043 Grenoble, France
[b] Helmholtz Centre Berlin, Institute of Applied Materials, D-14109 Berlin, Germany
[c] Technische Universität Berlin, D-10623 Berlin, Germany
[d] Institute for Synchrotron Radiation – ANKA, Forschungszentrum Karlsruhe, D-76021 Karlsruhe, Germany
[e] Bundesanstalt für Materialforschung und -prüfung, D-12205 Berlin, Germany

Received 2 April 2009; received in revised form 25 June 2009; accepted 26 June 2009
Available online 5 August 2009

Abstract

The mechanisms behind pore formation in aluminium alloys that are in commercial use for making foam components are still not understood. It is accepted that they play a key role in the quality of the evolving pore structure. In order to shed light on early pore formation, aluminium foams in low expansion stages made by the powder-compact melting process were investigated by synchrotron-based hard X-ray microtomography and quantitative image analysis. The calculated spatial correlation functions between the gas source (TiH_2 particles) and the nucleating pores show that the location of pore formation and the spatial gas source distribution for AlSi7 and Al–Si–Cu alloys are essentially independent. Therefore, in the alloys investigated, the position of the melt formation is found to determine the pore nucleation rather than the spatial distribution of TiH_2. This behaviour explains the known positive effect on the pore structure achieved by adding copper.

Keywords: Microtomography; Image analysis; CT; Aluminium foam; Aluminium alloy

1. Introduction

Replacement of engineering structures, e.g. in automobiles, by lightweight aluminium foam has been predicted several times in the past Ref. [1] and more recently [2], but many years after those initial predictions the market for aluminium foam is still small [3]. One reason for this is that the available aluminium alloy foams still do not have the required properties, partially owing to the fact that during foaming the evolving cellular structure contains more heterogeneities than would be expected from purely statistical scatter and more than are acceptable in practice. Therefore, research is been carried out that is aimed at improving the uniformity of the cell structure. To understand these irregularities, it is necessary to study the nucleation of pores and their evolution in the early stages of foam production.

This paper focuses solely on the foaming of aluminium alloys based on metal powders: metal and blowing agent powders are mixed and compacted, after which the compacted mixture is heated to a temperature high enough to ensure the melting and foaming of the alloy [4]. The blowing agent particles – usually TiH_2 – start to release gas (hydrogen), which leads to pore nucleation and subsequent pore growth. Mostly, highly expanded foams have been studied, whilst not much work has been done on early

* Corresponding author. Address: European Synchrotron Radiation Facility, BP220, F-38043 Grenoble Cedex, Isere, France. Tel.: +33 0 476 88 1781; fax: +33 0 476 88 2785.
E-mail addresses: arack@snafu.de (A. Rack), banhart@helmholtz-berlin.de (J. Banhart).

1359-6454/$36.00 © 2009 Acta Materialia Inc. Published by Elsevier Ltd. All rights reserved.
doi:10.1016/j.actamat.2009.06.045

stages of foam expansion when the solid precursor is just starting to increase its volume.

It was noticed early in metal foam development that the different alloys in use showed different foaming behaviour, pore shapes and size distributions. Two of the alloys used for the production of metal foam components at that time – the wrought alloy 6061 and the casting alloy AlSi7 – were studied by Duarte and Banhart [5], Baumgärtner et al. [6] and Mosler et al. [7]. Especially for AlSi7, extremely anisotropic foaming behaviour was found. Bellmann et al. [8] defined the problems, suggested suitable methods for investigating early stages of foaming and distinguished between two types for pore formation in metal foams:

type-I: local pore formation occurring at the location of individual blowing agent particles; and
type-II: non-local formation at other locations in the precursor material.

In a further step, AlSi7 was studied in more detail using synchrotron X-ray microtomography to determine non-destructively the size distribution of the pores in early stages as well as to analyse their morphology and connectivity [9]. A further advance was the description of the different pore formation mechanisms in both AlSi7 and 6061 alloy by employing microtomography with higher spatial resolution, and the observation not only of different pore morphologies but also of different correlations between the positions of the TiH_2 particles and the pore volume [10,11]. While in 6061 the TiH_2 particles were preferentially found near the inner pore surfaces, they were distributed almost randomly in AlSi7. It was concluded that in 6061 the pores are locally inflated around blowing agent particles (type I), whereas in AlSi7 the evolving hydrogen migrates to weak points in the matrix and creates pores there non-locally (type II). The suspicion that these weak points are defined by the Si particles in the pressed powder mixture (Al + Si) [7] was confirmed later by holographic tomography [12]. A further continuation of the work was undertaken subsequently and came in two parts. First, as the method of determining spatial correlations was based on standard morphological transformations, leading to a coarse grid of analysable distance values around the pore volume, the mathematical routines were reviewed. A new approach to access the distance values around the pore space was implemented and applied to 6061 and AlSi7 alloy foam in early stages, thus demonstrating the new method [13]. Secondly, and this is the topic of the present paper, new high-resolution data sets were analysed using the refined algorithm. Moreover, a number of new samples were manufactured for imaging with lower resolution but a greater field of view in order to increase the statistical significance of the conclusions derived. As in the meantime alloys from the alloy system Al–Si–Cu had emerged as the preferred materials for industrially produced foam sandwich cores [14,15], characterized by low melting points and more uniform pore size distributions, two alloys from this system were included in this study.

2. Methods

This section describes the preparation of the different specimens that were analysed, as well as the experimental and mathematical approaches used to investigate early pore formation in aluminium foams.

2.1. Sample preparation

The specimens investigated were made by foaming powder compacts, i.e. blends of elemental metal powders and TiH_2 powder. Table 1 summarizes the processing parameters used for the investigations in this work, namely composition, blowing agent content, pressing temperatures and pressures, and foaming temperature.

Some of the samples were prepared at the Fraunhofer Institute (IFAM), Bremen (Germany) and were cut to such dimensions that the foams could be imaged by synchrotron microtomography (SμCT) employing a high spatial resolution around 1 μm. The parameters that were varied included the alloy composition (AlSi7 vs. AlSi6Cu4), TiH_2 content (0.5 or 1 wt.%) and compaction temperature (200 and 450 °C). The lower compaction temperature was known to lead to insufficient compaction and expansion, while the higher temperature produces a virtually dense precursor material with a residual porosity $\leqslant$0.75% [5]. The results presented in this work are restricted to those sample series where at least four different expansion stages (see below) could be successfully investigated by SμCT. The samples in this series will be called IFAM-AlSi (1 and 2) and IFAM-AlSiCu. In all cases, the foaming process was triggered by heating the obtained precursor material in a pre-heated furnace (600 °C). Quenching the samples after various pre-defined dwell times in the furnace conserves pore structures in various expansion states [16,10]. The

Table 1
Overview of the sample series investigated, including their foaming and imaging parameters.

Sample series	Composition	Blowing agent	Compaction	Foaming (°C)	Image resolution (μm)
IFAM-AlSi-1	AlSi7	0.5 wt.% TiH_2	450 °C, 120 MPa	600	~1
IFAM-AlSi-2	AlSi7	1.0 wt.% TiH_2	200 °C, 120 MPa	600	~1
IFAM-AlSiCu	AlSi6Cu4	0.5 wt.% TiH_2	450 °C, 120 MPa	600	~1
TUB-AlSi	AlSi7	1.0 wt.% TiH_2	450 °C, 295 MPa	650	~10
TUB-AlSiCu	AlSi6Cu10	1.0 wt.% TiH_2	400 °C, 295 MPa	600	~10

highest temperatures reached during foaming can be estimated by comparison with measurements on samples of the same composition foamed in a previous work [5]. Depending on the expansion stage, this temperature ranges from 576 to 585 °C.

A second series of samples (TUB-AlSi and TUB-AlSiCu) was later prepared at Berlin University of Technology (TUB, Germany) in order to be investigated with SμCT employing spatial resolutions around 10 μm and correspondingly larger sample volumes and statistics. The production procedure was slightly improved compared to the manufacture of the IFAM samples, as higher compaction pressures could be applied. The foaming device used allowed more precise temperature and time control. Samples were quenched after expansion to different expansion levels in ice water [17]. The highest temperature reached in these experiments was measured by a thermocouple inserted into the sample for the Al–Si–Cu alloy (unlike in the previous IFAM experiments) and was about 525 °C for AlSi6Cu10, or slightly higher. For each parameter set of the TUB series, samples were produced by using non-treated TiH_2 and a heat-treated TiH_2 (3 h at 480 °C in air) that helps to avoid premature hydrogen evolution [18].

Samples for SμCT were prepared by electrodischarge machining (IFAM) as well as by sawing (TUB). The samples consisted of rods with a square cross-section of $1 \times 1\ mm^2$ for the [19,20] experiments and around $6 \times 6\ mm^2$ for the lower resolution.

2.2. Synchrotron microtomography

Experiments were carried out using the microtomography facilities at the European Synchrotron Radiation Facility's ID19 (ESRF) and the BAM*line* located at the light source BESSY-II at the Helmholtz Centre Berlin [21,22]. Owing to the availability of higher photon flux density, we scanned selected samples with highest resolution at ESRF and performed scans of a broader range of larger specimens with moderate resolutions at BESSY-II. Both facilities employ conventional high precision sample manipulators for the alignment and rotation of the specimen before as well as during the tomography scan. For high-resolution pixel detectors, the indirect approach based on the concepts of Hartmann et al. [19] and Bonse and Busch [20] is used. Here, a scintillating screen (powder or single crystal) converts X-rays into visible light. This luminescence image is captured by coupling a CCD chip optically with the scintillator. The indirect detection concept using thin single crystal film scintillators makes it possible to reach resolutions in the sub-micrometre range [23].

The high-resolution scans at ESRF were done utilizing a pixel size of 0.7 μm, leading to a true spatial resolution around 1.5 μm and a field of view of $1.4 \times 1.4\ mm^2$ (due to the 2048 × 2048 pixel "FReLoN 2000" type CCD camera used [24]). The maximal sample volume to be analysed with this setting would be $(1.4\ mm)^3$. The synchrotron beam was monochromatized to 17 keV which allowed for easy subsequent image analysis (see the next section).Thousand four hundred projection images were recorded during 180° scans in order to ensure high-quality reconstruction of the tomographic images [21].

Tomographic scans with a moderate resolution of around 12 μm (10% of the modulation transfer function, determined via a knife-edge scan) were performed at BESSY-II. As CCD camera, a Princeton Instruments, type VersArray:2048B was used, with an effective pixel size of 3.5 μm (2048 × 2048 pixels, effective $7 \times 7\ mm^2$ field of view, $(7\ mm)^3$ maximal sample volume to be analysed). Depending on the sample dimensions, the synchrotron beam was monochromatized to photon energies between 20 and 25 keV. Typically, 720–900 projection images were recorded during 180° scans [25].

Tomographic reconstructions were carried out using the conventional filtered back-projection algorithm. We chose to use the PyHST software package developed by the SciSoft group at ESRF [26] as it allows for the use of self-written filters as plugins. In order to improve the reconstruction quality, two filters – a median filter to reduce noise and a ring artefact filter based on a bandpass applied to the sinograms prior to backprojection – were coded as plug-ins in cooperation with the SciSoft group [27].

2.3. Three-dimensional (3-D) image analysis

Synchrotron microtomography delivers volume data sets as a 3-D matrix of numbers that can be interpreted as greyscales and thus appear as images. When working in absorption contrast mode, each matrix value represents the local attenuation of a voxel (acronym for "volume picture element"), which is related to the density and the attenuation coefficient of the material [28]. The greyscale information can be used to identify and subsequently separate different material phases inside the volume images, provided that a significant difference in the attenuation behaviour of the individual phases is given. For example, one can distinguish between aluminium and TiH_2 or Cu, while there is almost no absorption contrast between aluminium and silicon as, for example, at an X-ray energy of 17 keV the attenuation coefficients are: 13.5 cm^{-1} (Al), 15.3 cm^{-1} (Si), 110.8 cm^{-1} (Ti) and 471.3 cm^{-1} (Cu) [29]. In order to separate the different phases into independent Boolean images, where voxels belonging to the selected material are given the foreground value "1" and the remains are set to the background value "0", we use a greyscale threshold hysteresis in combination with a region growing algorithm [30]. Here, two thresholds are used to define a range in the image's histogram where voxels definitively belong to one phase, e.g. the pores. A second pair of thresholds defines a larger range in the histogram, selecting voxels that might belong to this phase. In successive stages the algorithm extends the voxels already identified as belonging to one phase, e.g. pores, by those that (i) contain a grey value in the second range defined and (ii) are direct neighbours of the already identified phase. The required

parameters are optimized manually in order to acquire Boolean images with minimal amounts of artefacts and noise. For some data sets, the morphological transformations *open* and *closure* are applied to the Boolean images to further reduce noise and artefacts [30,31].

The aim of our image analysis is to identify spatial correlations between the positions of the blowing agent particles and the positions of the pores inside aluminium foams at different expansion stages. The analysis is based on the Boolean images introduced above, here specifically the Boolean images of the pore space and the blowing agent particles. Our algorithm dilates the Boolean pore structure, creates the difference between the dilated and the original Boolean pore image and then calculates the density of the blowing agent particles in this differential volume (see Fig. 1). This procedure is repeated in successive steps until the dilated pore volume encompasses 99% of the total image volume. If the blowing agent density is high during the first dilation steps (close to the pore surface) and then decreases with ongoing dilation, there is a correlation between the pore surfaces and the blowing agent particles, identifying type I behaviour, as the majority of the blowing agent particles is located close the the pores. If the density remains constant for all dilation steps then there is no spatial correlation between pores and blowing agent, indicating type II behaviour; cf. Fig. 7.

Sometimes the density varies in an irregular way or even grows slightly as the distance to the pore surface increases. There is no reason to believe that TiH_2 particles should be preferentially found at a non-zero distance from the pores – or, at least, none that we are aware of. One might speculate that such apparent "negative correlations" between pores and TiH_2 densities stem from coarse spherical TiH_2 particles that are situated at the interfaces and have their maximum cross-section at a distance of half their diameter of, say, 20 μm. We prefer the viewpoint that such variations are unphysical and class them as "no correlation". The presence of various differently absorbing phases around the pores could give rise to spurious contributions to the distribution function. This viewpoint is supported by the observation that these "negative correlations" occur in intermediate stages of evolution, i.e. between "unfoamed" and "fully molten".

Care has to be taken to treat the interfaces between the pores and the metal. To avoid possible artefacts, a layer around each pore space of the thickness of the FWHM of the detector's point spread function is discarded from the analysed density data. A more detailed description of the algorithm, including a sound mathematical discourse, has been published elsewhere [13].

3. Results

In this section, the 3-D image analysis of volume data sets acquired at ESRF and BESSY-II will be presented in two parts, each dedicated to one of the two alloy families investigated. The high-resolution scans of selected samples are introduced first, followed by the analysis of the inter-

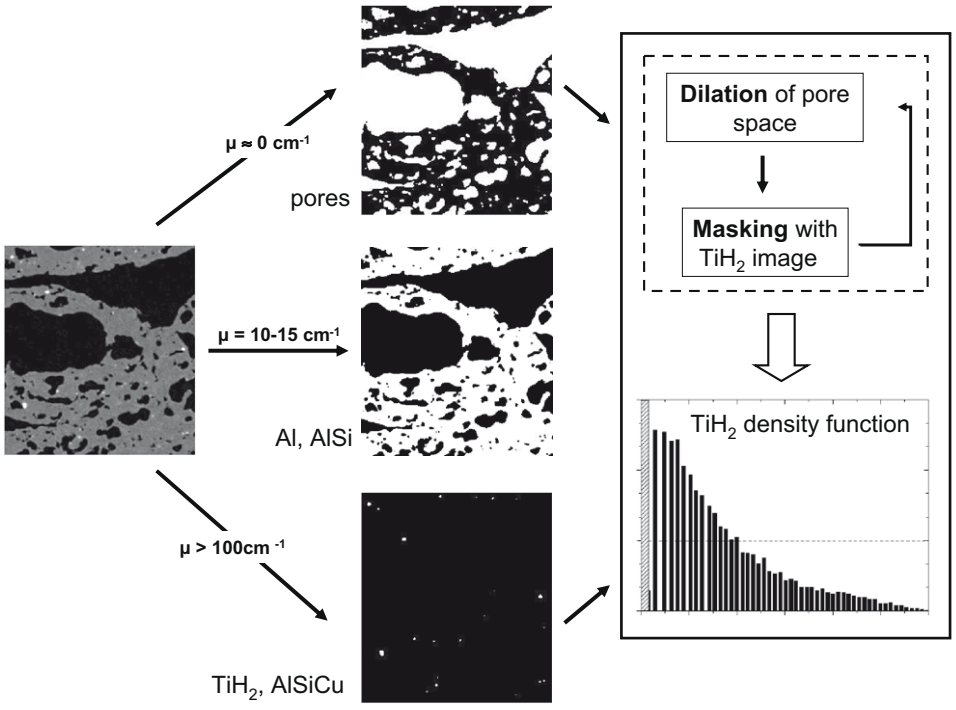

Fig. 1. Schematic representation of the correlation analysis applied, based on the segmentation of the greyscale image (left column) into Boolean images, representing, from the top to the bottom of the middle column, the pores, the metallic matrix and the blowing agent, plus – for Al–Si–Cu alloys only – highly absorbing parts of the metallic matrix. Only the former and latter are used for the final analysis (right column), whereas the Boolean image of the metallic matrix is not needed. The ranges given for the absorption coefficient μ are approximate and correspond to a photon energy of 17 keV.

mediate resolution scans, which are greater in number and underline the statistical relevance of our observations.

3.1. AlSi7 foams

The AlSi7 samples labelled "IFAM" were scanned at a high resolution of around 1.5 μm. The four specimens of the series IFAM-AlSi-1 compacted at 450 °C (60 s, 75 s, 90 s and 120 s dwell time in furnace) show porosities of 0.31%, 0.43%, 0.46% and 7.43% as determined by 3-D image analysis (see Fig. 2). The onset of foaming from the still dense material to the pore-containing state is therefore fairly immediate, taking place between 90 and 120 s after heating begins. Tomographic slices of the five IFAM-AlSi7-2 samples compacted at 200 °C (0, 60, 75, 90 and 120 s dwell time in the furnace) are displayed in Fig. 3. The respective (initial) porosities of 15.8%, 11.4%, 15.2%, 18.3% and 14.5% are significantly higher and more constant compared to the first four due to the lower compaction efficiency at 200 °C. The unfoamed precursor already contains porosity when this compaction temperature – generally regarded as insufficient for making foams – is applied, whereas the "normal" compaction temperature leads to a virtually dense precursor.

After the creation of Boolean images, the correlation analysis algorithm was applied, the results of which are displayed in Fig. 4 for the specimens compacted at the higher temperature. The quantity calculated is the blowing agent particle density (normalized to the mean density in the foam matrix) as a function of distance to the closest pore surface. No value can be given for the unfoamed precursor since this sample is nearly dense and no meaningful pore volume exists to which the TiH_2 density can be related. The range for which the correlation function can be given varies in Fig. 4 and in the subsequent figures in this paper. For geometrical reasons, the available pore space can be dilated more before meeting adjacent pores in dense samples. For the first three stages of foaming – all still associated with porosities well below 1% – the density function does not show any sign of preferential positioning of TiH_2 particles with respect to the surface of the pores. This means that the tiny first pores nucleate at any distance from the TiH_2 particles. Only in the last sample of the series (120 s dwell time, 7.4% porosity) is a high density visible close to the pore space (spatial correlation), and this then decays as the distance from the nearest pore surface increases, i.e. in this sample most of the pore volume is close to a blowing agent particle.

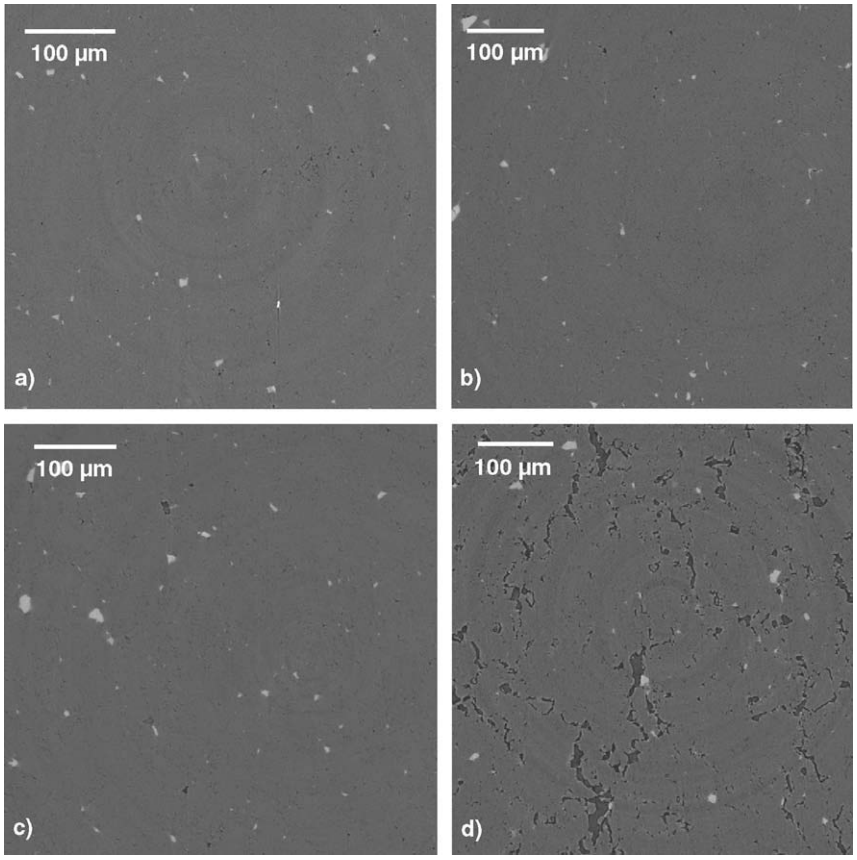

Fig. 2. Tomographic slices of the IFAM-AlSi-1 foam series (AlSi7 + 0.5 wt.% TiH_2 hot compacted at 450 °C) with pores in dark grey, metallic matrix in grey and blowing agent particles in white. Porosities with respective dwell times in the furnace are: (a) 0.31% (60 s), (b) 0.43% (75 s), (c) 0.46% (90 s) and (d) 7.4% (120 s). The orientations of compaction and foaming are perpendicular to the image plane. See also Fig. 4.

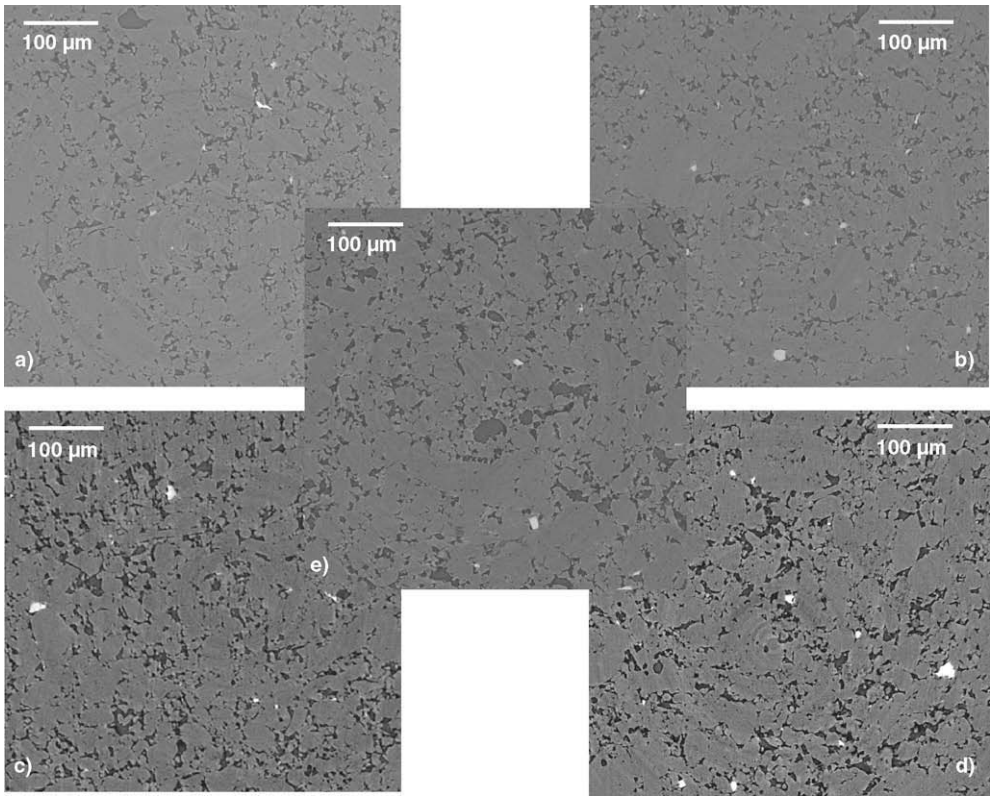

Fig. 3. Analogous to Fig. 2 for a 200 °C compaction temperature (IFAM-AlSi-2 series). Porosities with respective dwell times in the furnace are: (a) 15.8% (0 s), (b) 11.4% (60 s), (c) 15.2% (75 s), (d) 18.3% (90 s) and (e) 14.5% (120 s). The orientations of compaction and foaming are perpendicular to the image plane. See also Fig. 5.

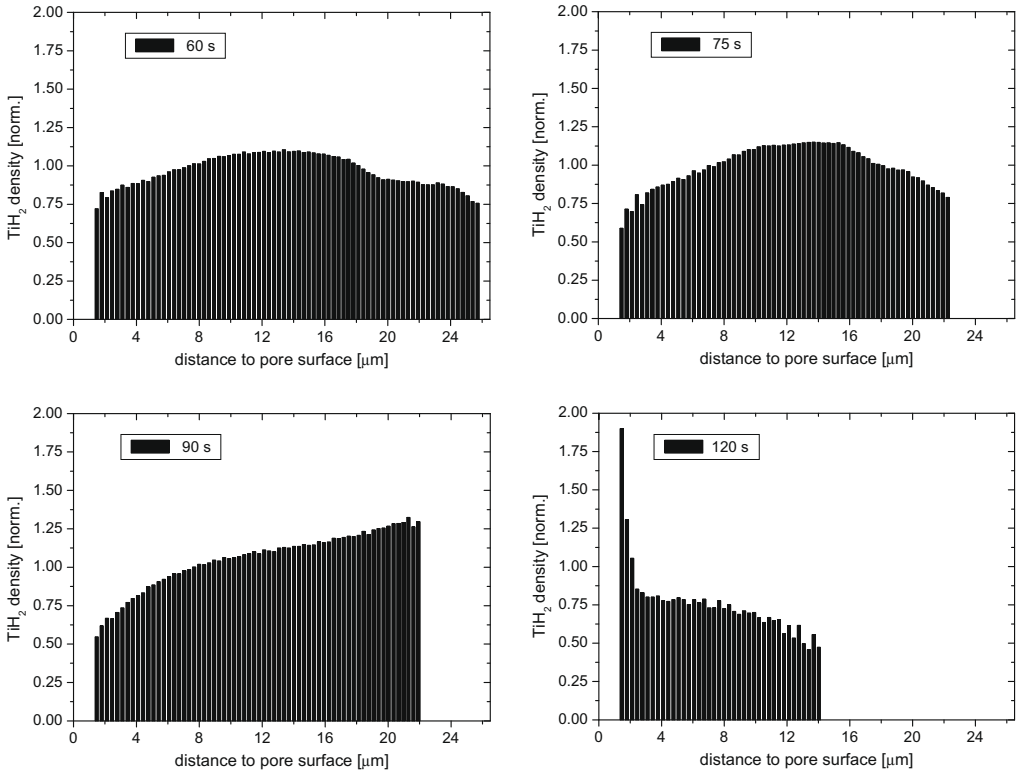

Fig. 4. Spatial correlation between pore volume and TiH_2 particles of the AlSi7 + 0.5 wt.% TiH_2 samples (IFAM-AlSi-1 – precursor material hot compacted at 450 °C, SμCT volume images acquired with high spatial resolution). The TiH_2 density is normalized to the mean density found in the foam matrix. Data for distances <1.5 µm are omitted due to the limitation given by the resolution. The graphs are arranged in the same way as in Fig. 2.

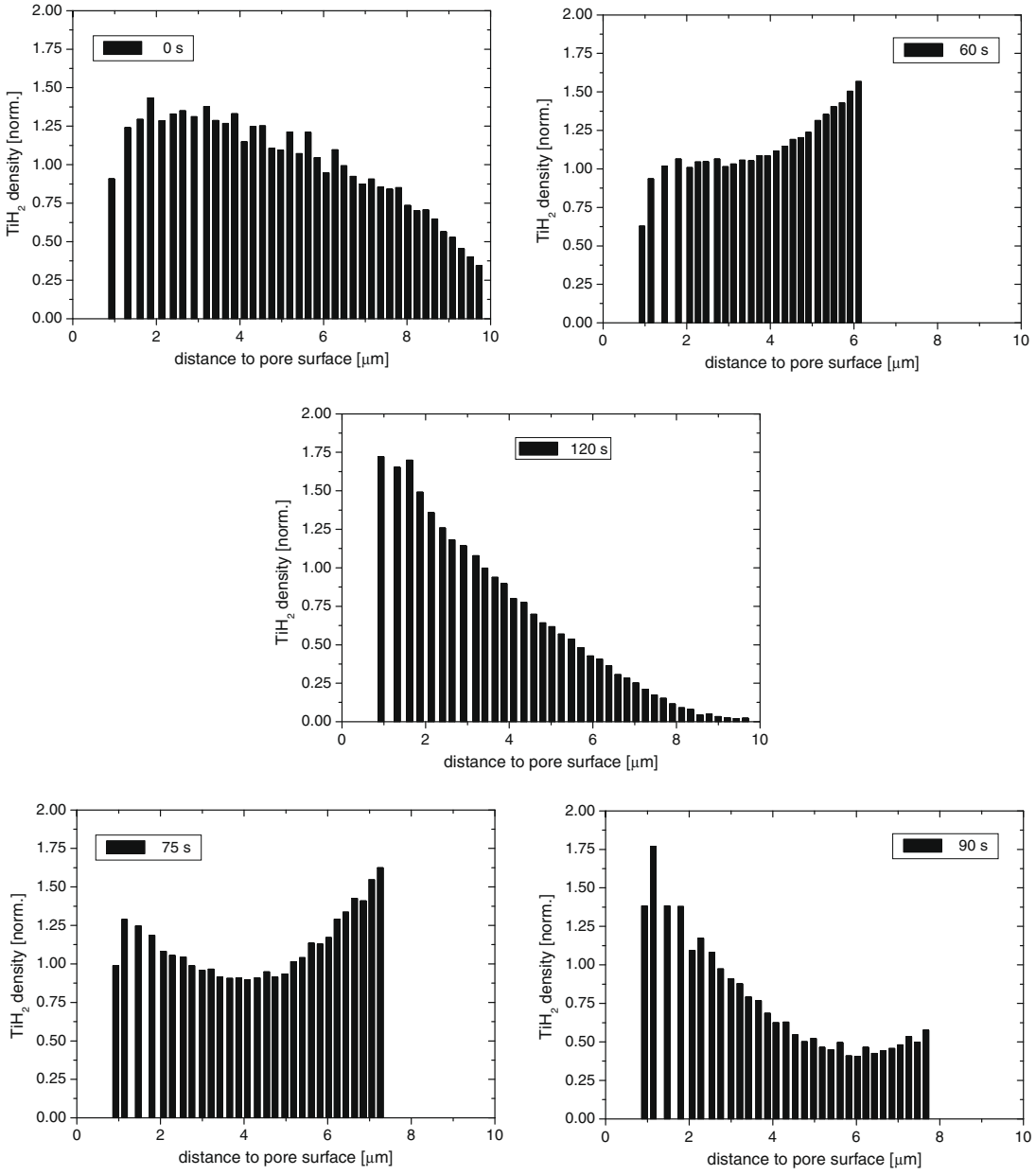

Fig. 5. Same as Fig. 4 for samples hot compacted at 200 °C (IFAM-AlSi-2, SμCT volume images acquired with high spatial resolution). The data for distances <1.5 μm are omitted due to the limitation given by the resolution. Graphs are arranged in the same way as in Fig. 3.

With the 90 s dwell time and also in a number of other data sets in the rest of the article, there is even a slight increase in density as the distance to the pore space increases. Such increases do not correlate with any direct observation of the foams by microscopy and, together with minor variations as in the first two curves, will be considered irrelevant in the following, although no clear reason for these variations could be identified.

The correlation was also observed for the other series (see Fig. 5), where the compaction temperature was deliberately set too low. The difference here is that the unfoamed state already contains 15% porosity and can therefore be used for the correlation analysis. The density curve is almost horizontal for this sample, as it should be for a random powder mixture, and the fluctuations still observed provide an estimate for the error of the analysis. Heating for 60 and 75 s does not change the picture very much. Except for a slight indication of the artefact already mentioned, there is no sign of big changes in the distribution function. No sign is found that TiH_2 particles preferentially segregate near the pore surfaces. Only after the longer heat treatments (90 and 120 s in the furnace) does the density of the blowing agent particles close to the pore space increases at the cost of the locations far away from the surface, i.e TiH_2 is segregated to the surface.

In order to validate these findings, which were based on a small number of low-volume samples, we investigated further AlSi7 foam samples – the TUB-AlSi series. These larger samples were imaged with a lower resolution (corresponding to a larger pixel size and, hence, a larger field of

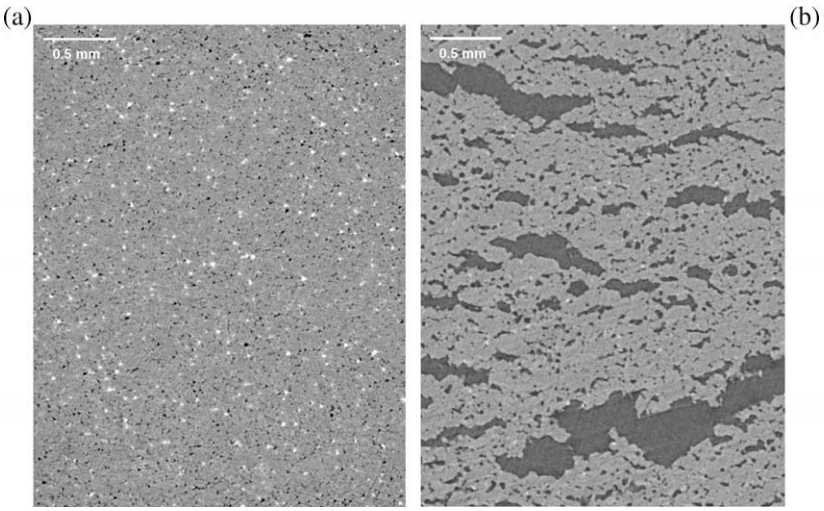

Fig. 6. Sample slices from the AlSi7 + 0.5 wt.% TiH_2 (TUB-AlSi) foam series with heat-treated TiH_2 used as blowing agent (SμCT volume images acquired with moderate spatial resolution). The pores are dark, the metallic matrix is grey and the blowing agent appears in white. (a) 1.5% porosity, (b) 28% porosity; cf. Figs. 7 and 8. The orientations of compaction and foaming are parallel to the image plane [25].

view of the detector), while the resolution was still sufficient to distinguish between correlated and uncorrelated TiH_2 distributions. Of the 23 samples in this series, 12 can be considered as early stages, with porosities ranging from 1% to 6%, while the remaining 11 samples are in more expanded foaming stages, with porosities between 15% and 50%. Typical tomographic slices can be seen in Fig. 6. Our analysis revealed that in 11 out of the 12 early-stage AlSi7 foam specimens no segregation of TiH_2 particles to the pore surfaces could be observed, while, in contrast, all of the more expanded AlSi7 foam samples showed a clear segregation. In other words, in the early stages of foam expansion of this alloy the pores are generated and inflated anywhere in the sample without necessarily being close to the gas-generating TiH_2 particles (type II), whereas in the later stages most of the TiH_2 particles are found very close to the pores' surfaces (type I).

Two typical correlation plots from the TUB samples showing the two limiting cases can be found in Fig. 7. In

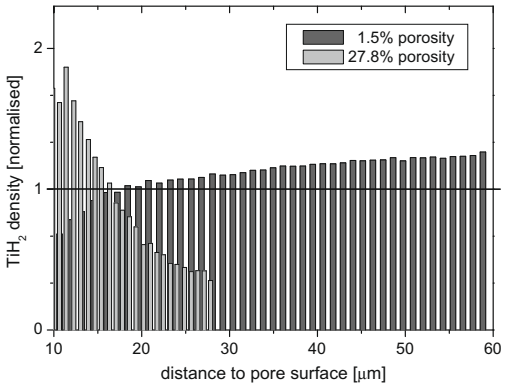

Fig. 7. Correlation analysis of the two samples from the TUB-AlSi foam series shown in Fig. 6. The data for distances <10 μm are omitted due to the limitation given by the resolution.

the early foaming stage corresponding to 1.5% porosity, the density of the blowing agent particles is only weakly dependent on the distance to the pore space, indicating the absence of segregation. In the more extended stage – 28% porosity – the density distribution of the blowing agent particles shows a clear spatial correlation between TiH_2 and the pore space (see also Figs. 6 and 8). The increase in the curve corresponding to the lower density (from 0.7 to 1.2) is again seen as an artefact and is indeed markedly lower than the decrease in density for the more expanded sample from 1.85 to 0.35. For a complete listing of tomographic slices and correlation plots see Appendix D of Ref. [25].

The nature of type II pores in AlSi7 foam can be better understood by taking a look at cut, polished and etched specimens by light microscopy. Etching makes it possible to distinguish between former powder particles more easily. In Fig. 8a a metallographic image of an AlSi7 foam from the TUB batch in the early stage – 1.5% porosity – is shown. In the vicinity of the TiH_2 particles, pores can only be found if silicon particles are also in the neighbourhood, while the majority of pores are located directly adjacent to silicon particles or silicon particle clusters, i.e. the silicon particles define the positions of the pores. In contrast, in an extended stage with 28% porosity (see Fig. 8b), most of the then much larger pores are located around or close to blowing agent particles.

3.2. AlSi6Cu4 and AlSiCu10 foams

Four IFAM-AlSiCu specimens with the nominal composition AlSi6Cu4 + 0.5 wt.% TiH_2 were imaged with the high-resolution (around 1.5 μm) setup at ESRF. The respective dwell times in the pre-heated furnace for these samples were 0, 60, 90 and 120 s, i.e. the precursor and three foamed states were investigated. Tomographic slices

of the 0, 90 and 120 s sample are displayed in Fig. 9. Because of the high stopping power of pure copper, the volume images of the 0 and 60 s samples contain so many artefacts in the form of white streaks that these images cannot be interpreted more than qualitatively. After 90 s, most of the copper has obviously been dissolved in the melting aluminium (see Fig. 9b). A moderately absorbing mixed-phase and the first pores can now be seen at the positions of former copper particles. In addition, several TiH_2 particles in the slice can be identified between the positions of former copper particles. Pores only seem to be inflated at those positions that appear in light grey, i.e. the copper particles define the positions of the pores. The volume image of the specimen after 120 s of heat-treatment was the only one that was artefact-free (see Fig. 9c) and allowed for a correlation analysis.

We separated all highly absorbing material (TiH_2 and Al–Si–Cu mixed phase, about 0.32% mass fraction/0.20% volume fraction) into one Boolean image and the pore space (6.1% porosity in this sample) into another. The result of the correlation analysis is plotted in Fig. 10. Two peaks can be distinguished: one close to the pore surface and a second one at a distance of approximately 29 μm from the pore surface. From the tomographic slices in Fig. 9 we identify the first maximum with the mixed phase

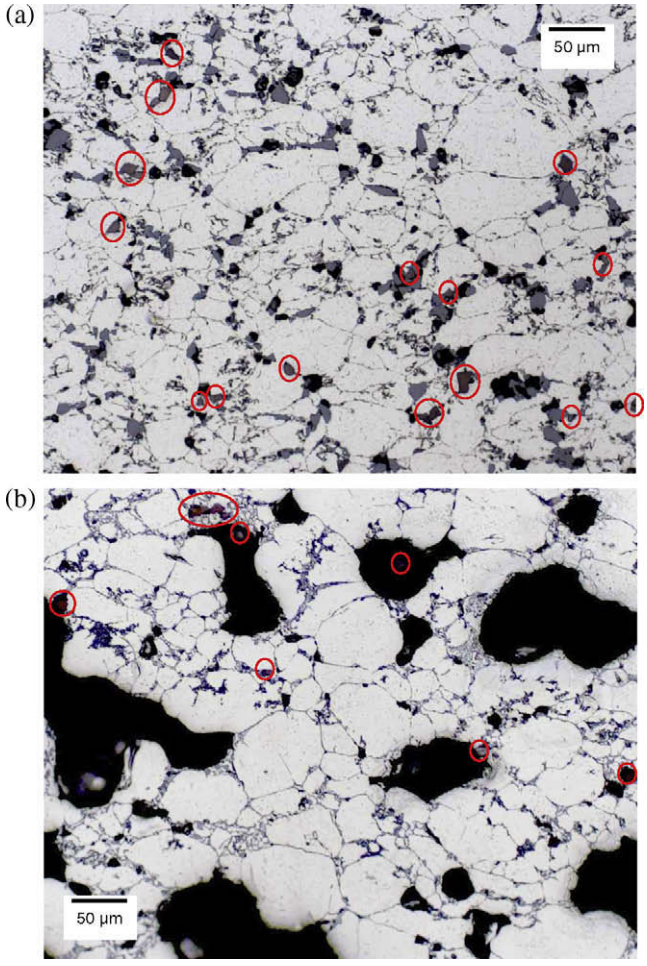

Fig. 8. Metallographic image of AlSi7 + 0.5 wt.% TiH_2 (TUB-AlSi) samples in two foaming stages: (a) the early stage with 1.5% porosity (discussed also in Ref. [13]) and (b) the later stage with 28% porosity. Both samples were etched with 0.5% HF. Aluminium particles appear in light grey, silicon particles in medium density grey and TiH_2 particles are marked with circles. Cf. Figs. 6 and 7.

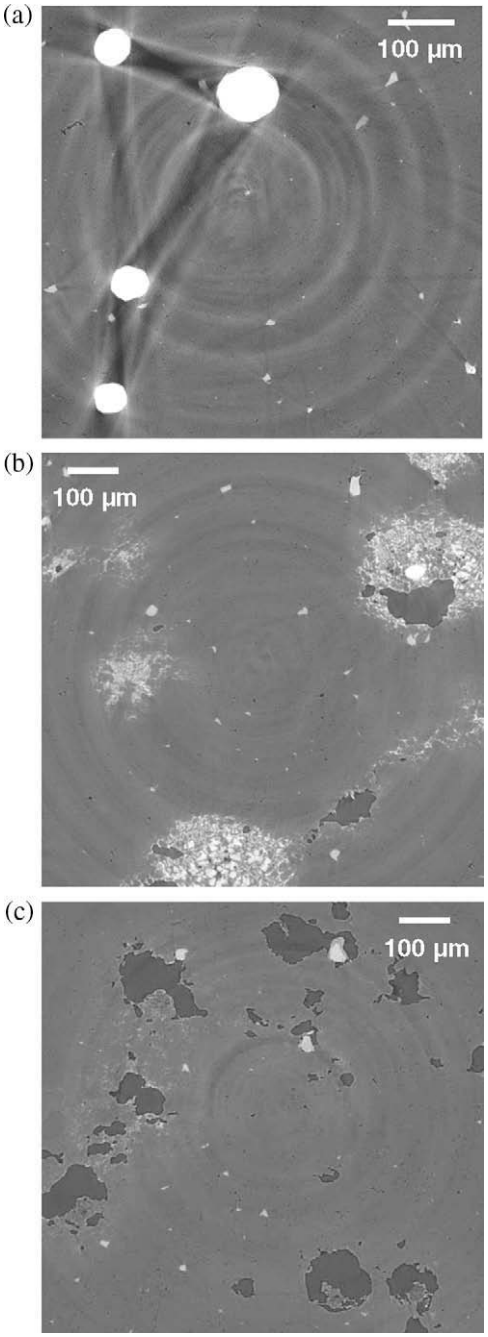

Fig. 9. Tomographic slices of IFAM-AlSiCu specimens (AlSi6Cu4 + 0.5 wt.% TiH_2, hot compacted at 450 °C, SμCT volume images acquired with high spatial resolution). White represents Cu, light grey TiH_2, medium grey metal, dark grey pores: (a) Raw precursor material with strong artefacts originating from the copper particles; (b) state after 90 s of heat treatment, showing that copper has been largely dissolved and the first pores have appeared and (c) state after 120 s, showing that there is no more Cu, and that the remaining highly absorbing particles are TiH_2 (6.1% porosity). See also Fig. 10.

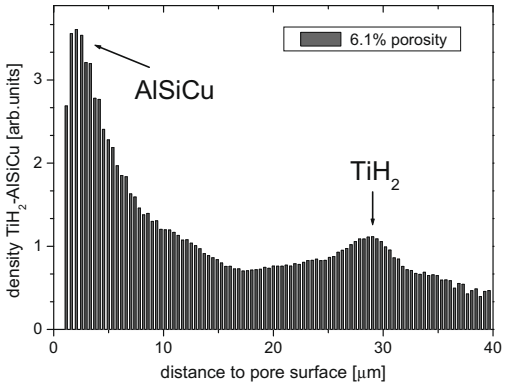

Fig. 10. Correlation analysis of an IFAM-AlSiCu specimen (AlSi6Cu4 + 0.5 wt.% TiH_2 hot compacted at 450 °C) after 120 s of heat-treatment: the density of highly absorbing material (aluminium–copper alloy and TiH_2) is plotted vs. its distance to the pore surface. See also Fig. 9c. The data for distances <1.5 μm are omitted due to the limitation given by the resolution.

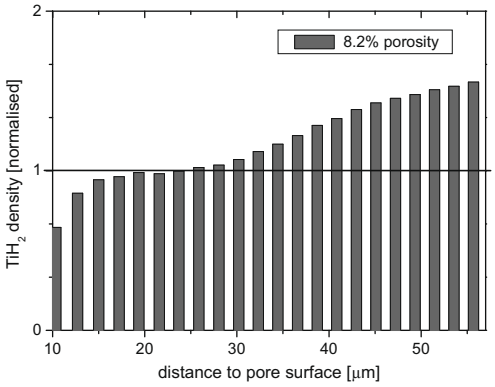

Fig. 11. Correlation analysis of a TUB-AlSiCu specimen (AlSi6Cu10 + 1.0 wt.% TiH_2). The density of the blowing agent particles is almost constant for all distances to the pore surface, indicating a lack of clear spatial correlation between the positions of the pores and the TiH_2 particles. The data for distances <10 μm are omitted due to the limitation given by the resolution.

(Al–Si–Cu), while the second maximum is mainly caused by the TiH_2 particles in the foam. Although more difficult to interpret, the tomographic scans of the IFAM AlSi6Cu4 + 0.5 wt.% TiH_2 samples point towards type II behaviour, i.e. pores are preferentially surrounded by Cu-rich aluminium melt, while the blowing agent particles can be at some distance from the pores and in fact may even be preferentially sited around 30 μm away from the gas/metal interfaces. Unlike AlSi7, the interpretation of these correlation curves requires some previous knowledge taken from metallographic sections (see below) because the value for the X-ray absorption coefficient of the mixed phase (Al–Si–Cu) can be very similar to that of TiH_2.

In analogy to the previous section, we scanned a larger batch of samples at moderate resolutions and higher sample volumes at BESSY-II, the TUB-AlSiCu series. The best and most consistent results were obtained for an alloy with an increased copper content that will be presented here. Altogether, volume images of 16 AlSi6Cu10 + 1.0 wt.% TiH_2 could be acquired and analysed. In five out of 16 samples the porosity is between 4% and 11% (early stage) and the TiH_2 contrast is high enough so that a correlation analysis is possible. None of these five samples show a spatial correlation in the sense of segregation of the blowing agent to the pore surface, thus indicating type II pores. In Fig. 11 an exemplary plot of the correlation analysis from this sample series can be found. Here, the Al–Si–Cu peak is not visible as in Fig. 10, possibly due to the lower resolution of the imaging system used and the higher Cu content in this alloy, which increases the signal from the Cu-rich phase. The density of highly absorbing material is nearly constant throughout the volume and no spatial correlation between this material and the pore space can be found. Again, for a complete listing of tomographic slices and correlation plots, see Appendix D of Ref. [25].

As for AlSi7, metallographic images are used to obtain additional information. In the image showing the raw precursor material (see Fig. 12a), the round copper particles, silicon particles and aluminium are visible. After 90 s of heat-treatment (see Fig. 12b), the copper particles have dissolved in the evolving melt and in their positions the first pores have now appeared. We performed EDX analysis in the vicinity of such an early pore in the IFAM sample, heat treated for 90 s (see Fig. 13). The high content of copper found close to and inside the pore confirms the observation that the pore surfaces are decorated with copper-rich eutectic melt. The metallographic image of the IFAM sample heat-treated for 120 s given in Fig. 12c illustrates the type II nature of the pores in AlSi6Cu4 foam – early pores inflate at the positions of former copper particles, sometimes far away from the TiH_2 particles.

Although the number of tomographic data sets that could be used for correlation analysis was much lower for this alloy than for AlSi7 – mainly because we could not identify the blowing agent with certainty in many of the samples – we find firm evidence that pores are of type II in this foam too, but no transition to type I is observed in the later stages of foaming.

4. Discussion

The experimental evidence provided by the work presented here confirms earlier observations that pore formation in metallic foams varies with the type of aluminium alloy chosen. A new alloy type – ternary Al–Si–Cu alloys – was investigated and yet another pore formation type found. The simple direct pore inflation mechanism identified in alloy 6061 alloys by Helfen et al. [10] and explained schematically in Fig. 14a was not found in any of the alloys studied here.

For AlSi7, the earlier observation that pores are not formed directly around the blowing agent particles as would be expected is confirmed by the correlation analysis (Figs. 4 and 5) and the two-dimensional metallographic

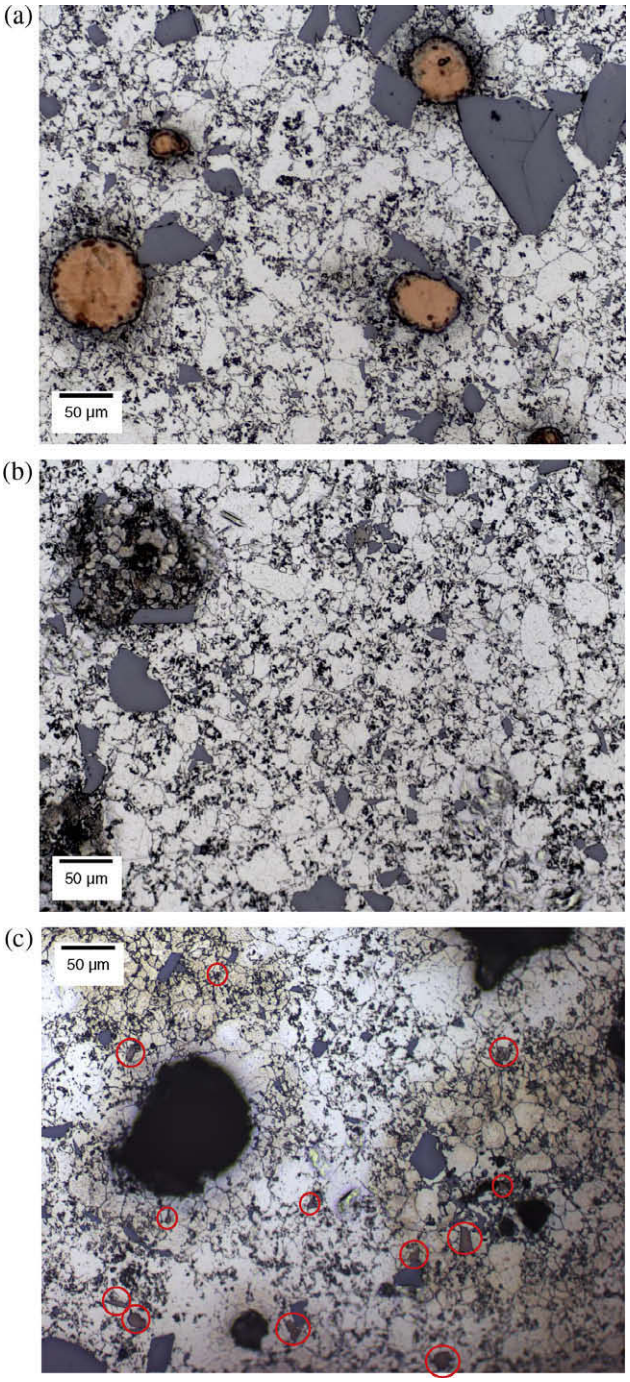

Fig. 12. Metallographic images of some IFAM-AlSiCu samples (AlSi6Cu4 + 0.5 wt.% TiH_2, hot compacted at 450 °C, sample surfaces etched with 0.5% HF): (a) raw precursor material (0 s heat-treatment); (b) 90 s of heat treatment; (c) 120 s of heat treatment. Copper appears in orange, silicon in blueish-grey, aluminium in white-grey and pores are dark. TiH_2 particles are marked by red circles in (c). See also Fig. 9. (For interpretation of the references to colour in this figure legend, the reader is referred to the web version of this article.)

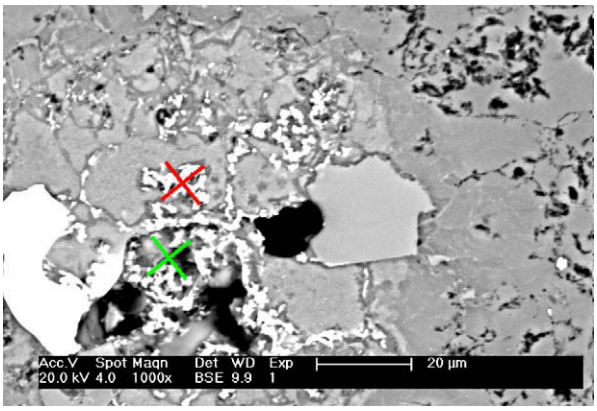

Fig. 13. SEM close-up of the sample shown in Fig. 12b. EDX analysis was performed at the positions marked. Red cross: 57 wt.% aluminium, 12 wt.% silicon and 31 wt.% copper; green cross: 94 wt.% aluminium, 4 wt.% copper and 2 wt.% silicon. The large white particle at the left border is copper; the one to the right of the pore (in the centre of the image) was identified as a silicon particle. (For interpretation of the references to colour in this figure legend, the reader is referred to the web version of this article.)

sections. The idea that most pores form in the vicinity of silicon particles is supported by metallography (Fig. 8 and Ref. [7]) – but only on a non-representative basis – and by the holotomographic correlation analysis presented by Helfen et al. [12], though only two samples were studied there. The combined evidence, however, now makes it very likely that the reason for this pore formation mechanism is that pores open at the weakest point in the metallic matrix, which in this case is the Al/Si interface. As gas is being generated by the TiH_2 particles, this gas can be transported to other parts of the foamable precursor, e.g. along the boundaries between the former powder particles, or through microchannels in the oxide films around these particles, etc. There it can create a gas pressure even at locations some tens of micrometres away from the blowing agent particle. As soon as the pressure exceeds the delamination threshold of the Al/Si interface, which is significantly reduced due to local melting of Al/Si eutectic, a pore opens there.

A new finding of the current work is that there is a transition from type II to type I behaviour during the evolution from an early stage to a later one, though this is still far away from full expansion. The exact reason for this transition is not clear. It is possible that, in the course of the formation of pores – which in AlSi7 are very jagged and often crack-like – a system of dense interconnected cracks evolves that then propagates through the entire sample. Helfen et al. [9] found that this crack system can be very extensive and interconnects a large volume of the sample. If, in addition, the cracks propagate preferentially along the TiH_2 particles and not through the bulk of aluminium, most of the TiH_2 particles would then be very close to the next open volume and create the type I behaviour observed. This can only be explained by an expansion of the open void space that eventually reaches all TiH_2 particles (visualized in Fig. 14b).

This idea can also provide an explanation for the poor foamability of insufficiently pressed powders, such as the ones used in Figs. 3 and 5. In these samples compacted at 200 °C, the change from type I to type II behaviour takes

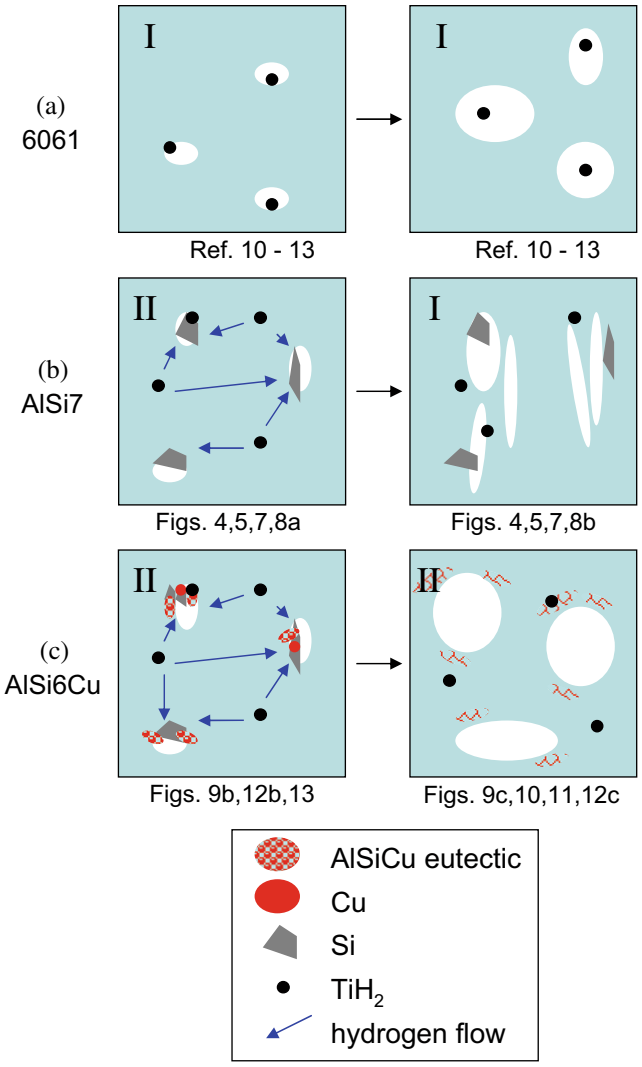

Fig. 14. Schematic summary of pores formation in different alloys (including alloy 6061) studied elsewhere [10–13]. The predominant pore formation type is given for each of the states, together with the images and figures supporting a given representation.

place earlier than in the samples compacted at 450 °C (see Fig. 2), and the correlation sunsequent is much more pronounced. As the interparticle bonding is weaker in the insufficiently pressed sample, the opening and propagation of cracks is more easily initiated by the internal pressure built up by the evolving blowing gas. The blowing agent particles are then connected to the large network of cracks and pores from an earlier stage, which in turn leads to a more serious loss of blowing gas.

The behaviour of the Al–Si–Cu alloy is different from that of the AlSi7 alloy. Both alloys share the feature that pore formation is not at the blowing agent site – i.e. type II – but at the weakest point in the matrix, which is not the Al/Si interface this time but the ternary eutectic melt that is formed at much lower temperatures than the binary eutectic in AlSi7, namely at 525 °C compared to 577 °C. As the sample expands further, the evolving liquid continuously wets the aluminium grains and significantly reduces the excessive formation of cracks [32]. Therefore, the pores can continuously grow in a fairly spherical way within the increasingly large pool of liquid metal.

In a wider context, these findings explain why Al–Si–Cu foams actually exhibit better foaming behaviour than AlSi7 and have replaced AlSi7 as core materials for aluminium foam sandwich panels [15]. First of all, the blowing agent releases gas at temperatures at which the matrix starts to melt and then delivers gas into a pool of liquid where it can form around pores – governed by surface tension – instead of the gas forcing the still solid material apart and propagating cracks through the material, as happens in AlSi7. The situation in AlSi7 is also more unfavourable because melting takes place at a higher temperature (577 °C) than in Al–Si–Cu (525 °C) and therefore the hydrogen pressure generated by the decomposing blowing agent is higher [18], [33]. Although such cracks round off after the metal has melted, as X-ray radiographic images show [34], they may lead to partial gas losses in the heating stage and give rise to the more heterogeneous pore morphology and size distribution generally observed in AlSi7 foams.

Looking to the future, the foaming behaviour of aluminium alloys could be further improved by tailoring the alloy composition so that either the ternary eutectic temperature is lowered – by further alloying elements – or the amount of melt immediately available after melting is increased by tuning the composition of the ternary alloy [33]. This would allow the blowing agent to feed gas into the evolving liquid continuously, thus keeping the pores spherical.

5. Conclusions

We confirmed a previous observation that AlSi7 foam develops type II pores in the first stage, i.e. the pores form at the weakest links in the pressed powder, the Al/Si interfaces. An improved statistical analysis based on 27 samples and a quantitative evaluation based on correlation analysis has been given. A new finding is the change from type II to type I pores in the following stage of foaming in AlSi7.

In addition to Al–Si, two alloys of the common and industrially applied Al–Si–Cu alloy family have been investigated. In these alloys, the pores first form along the liquid ternary eutectic around individual copper particles, which is then the weakest part of the material. These pores are therefore of type II and remain so even in the later stages when the porosity increases to ≈10%.

The sequence of pore formation with rising temperature in three different alloys (including 6061 from the literature) is summarized in Fig. 14 and can be described as follows:

6061: Hydrogen gas from blowing agent evolves → local pressure build-up around particles → melting of matrix → pore expansion around TiH_2 particles [10].

AlSi7: Hydrogen gas from blowing agent evolves → debonding at Al/Si interfaces and local melting of Al/Si eutectic → hydrogen pressure expands pore space at Si particles → further opening of pore space that eventually reaches most of the TiH_2 particles → complete melting of matrix.
Al–Si–Cu: Ternary eutectic melts → hydrogen gas from blowing agent evolves → pores nucleate along ternary melt pools and expand.

An interpretation of the favourable foaming characteristics of Al–Si–Cu alloys is now accessible and the criteria for selecting further alloys are clearer.

Acknowledgements

Various persons supported us during this work: H. Kropf prepared microscopic images, A. Haibel (HMI), P. Pernot (ESRF), G. Weidemann and H. Riesemeier (both at BAM) helped with the experiments, S. Mechler did the EDX analysis, H. Stanzick (Fraunhofer IFAM) prepared some of the foams, and J. Ohser (Hochschule Darmstadt) and K. Schladitz (Fraunhofer IWTM) worked jointly with us on the volume image analysis algorithms. The image analysis was performed using Fraunhofer ITWM's MAVI software [35].

References

[1] Niebylski LM, Fanning RJ, editors. Metal foams as energy absorbers for automotive bumpers, vol. 720490 of SAE Transactions. New York (USA): Society of Automotive Engineers, Inc.; 1972.
[2] Yu M, Eifert HH, Banhart J, Baumeister J. Mater Res Innov 1998;2(3):181.
[3] Lefebvre LP, Banhart J, Dunand DC. Adv Eng Mater 2008;10(9):775.
[4] Banhart J. Prog Mat Sci 2001;46:559.
[5] Duarte I, Banhart J. Acta Mater 2000;48:2349.
[6] Baumgärtner F, Duarte I, Banhart J. Adv Eng Mater 2000;2:168.
[7] Mosler U, Müller A, Baum H, Martin U, Oettel H. Microstructure of foamable precursor and foamed aluminium material. In: Banhart J, Ashby M, Fleck N, editors. Cellular Metals and Metal Foaming Technology. Bremen: MIT-Verlag; 2001. p. 233.
[8] Bellmann D, Banhart J, Clemens H. Acta Mater 2001;49:3409.
[9] Helfen L, Baumbach T, Stanzick H, Banhart J, Elmoutaouakkil A, Cloetens P. Adv Eng Mater 2002;4:808.
[10] Helfen L, Stanzick H, Ohser J, Schladitz K, Pernot P, Banhart J, et al. Investigation of the foaming process of metals by synchrotron-radiation imaging. In: Meyendorf N, Baaklini GY, Michel B, editors. Proceedings SPIE: testing, reliability, and application of micro- and nanomaterial systems, vol. 5045; 2003. p. 254.
[11] Helfen L. Investigation of the structure, formation and properties of porous, cellular and low-density materials with synchrotron-radiation imaging. Universität des Saarlandes; 2003.
[12] Helfen L, Baumbach T, Pernot P, Cloetens P, Stanzick H, Schladitz K, et al. Appl Phys Lett 2005;86:231907.
[13] Rack A, Helfen L, Baumbach T, Kirste S, Banhart J, Schladitz K, et al. J Microsc 2008;232(2):282.
[14] Anon. Website of Alulight International GmbH, Austria; 2009. <http://www.alulight.com/>.
[15] Banhart J, Seeliger HW. Adv Eng Mater 2008;10:793.
[16] Stanzick H, Wichmann M, Weise J, Banhart J, Helfen L, Baumbach T. Adv Eng Mater 2002;4:814.
[17] Bütow A. Strukturuntersuchungen an Metallschäumen in verschiedenen Entwicklungsstadien. Technical University Berlin; 2004. [in German]. <http://www.hmi.de/bereiche/SF/SF3/guests/diploma_%20buetow.pdf>.
[18] Matijasevic-Lux B, Banhart J, Fiechter S, Görke O, Wanderka N. Acta Mater 2006;54:1887.
[19] Hartmann W, Markewitz G, Rettenmaier U, Queisser HJ. Appl Phys Lett 1975;27:308–9.
[20] Bonse U, Busch F. Prog Biophys Molec Biol 1996;65:133.
[21] Cloetens P, Ludwig W, Baruchel J, Van Dyck D, Van Landuyt J, Guigay JP, et al. Appl Phys Lett 1999;75:2912.
[22] Rack A, Zabler S, Müller BR, Riesemeier H, Weidemann G, Lange A, et al. Nucl Instr Meth Phys Res A 2008;586(2):327.
[23] Koch A, Raven C, Spanne P, Snigirev A. J Opt Soc Am 1998;15:1940.
[24] Labiche JC, Mathon O, Pascarelli S, Newton MA, Ferre GG, Curfs C, et al. Rev Sci Instr 2007;78:0901301.
[25] Rack A. Charakterisierung komplexer Materialsysteme mittels Synchrotron-Tomographie und 3D-Bildanalyse. Technical University Berlin; 2006. [in German]. Available from: <http://opus.kobv.de/tuberlin/volltexte/2006/1370>.
[26] Mirone A, Wilcke R, Hammersley A, Ferrero C. PyHST – High speed tomographic reconstruction; 2009. <http://www.esrf.eu/UsersAndScience/Experiments/TBS/SciSoft/>.
[27] Banhart J, editor. Advanced tomographic methods in materials research and engineering. Oxford: Oxford University Press; 2008.
[28] Flannery PB, Deckmann HW, Roberge WG, D'Amico KL. Science 1987;237:1439.
[29] del Rio MS, Dejus RJ. XOP: recent developments. In: Macrander AT, Freund AK, Ishikawa T, Mills DM, editors. Proceedings SPIE: crystal and multilayer optics, vol. 3448; 1998. p. 340.
[30] Lohmann G. Volumetric image analysis. Chichester, New York: Wiley-Teubner; 1998.
[31] Elmoutaouakkil A, Salvo L, Maire E, Peix G. Adv Eng Mater 2002;4:803.
[32] Matijasevic-Lux B, Banhart J. Scripta Mater 2006;54:503.
[33] Helwig HM. Einfluss von Verdichtungsparametern und Legierungselementen auf das Schäumverhalten von Aluminiumpulverpresslingen. Technical University Berlin; in press [in German].
[34] Banhart J, Stanzick H, Helfen L, Baumbach T. Appl Phys Lett 2001;78:1152.
[35] Fraunhofer ITWM, Department of Image Processing. MAVI – modular algorithms for volume images; 2005. <http://www.itwm.fhg.de/mab/projects/MAVI/>.